

Deciphering the nature of temperature-induced structural phases of MAPbBr₃ by *ab initio* molecular dynamics*

Sayan Maity¹, Suraj Verma¹, Lavanya M. Ramaniah^{2,3}, Varadharajan Srinivasan¹

¹Department of Chemistry, Indian Institute of Science Education and Research Bhopal, Bhopal 462 066, India

²High Pressure and Synchrotron Radiation Physics Division,

Bhabha Atomic Research Centre, Trombay, Mumbai 400085, India and

³Homi Bhabha National Institute, Mumbai 400094, India

We present an *ab initio* molecular dynamics study of the temperature-induced structural phases of methylammonium lead bromide. We confirm that, the low-temperature phase is not ferroelectric and rule out the existence of any overall polarization at 40, 180, and 300 K arising from the motion of the individual sub-lattices. Our simulations at the room temperature resulted in a cubic $Pm-3m$ phase with no discernible local orthorhombic distortions. We trace the origin of possible octahedral distortions to an octahedral scissoring mode which nevertheless is ineffective in stabilising these distortions at room temperature. The predicted timescales of methylammonium motion agree very well with experimental estimates establishing dynamic disordering of the molecular dipoles over several orientational minima at room temperature. We also identify the key modes of the inorganic and organic sub-lattices that are coupled at all temperatures mainly through the N-H...Br hydrogen-bonds. Estimated lifetimes of the H-bonds are in good agreement with the timescales of methylammonium dynamics indicating a strong connection between these two aspects of organic inorganic hybrid perovskites.

I. INTRODUCTION

Organic-inorganic hybrid perovskites (OIHPs) indicated by chemical formula ABX₃ form an interesting class of systems where an inorganic lattice (B cation and X anion) hosts an organic cation (A) filling space inside the lattice. Recently, OIHPs, including MAPbBr₃ (MA=CH₃NH₃⁺) have shown great promise in solar cell technology due to high photo conversion efficiency (PCE) up to to 20% [1–13]. Various interesting dynamical phenomena such as Raman central peak, Rashba effect, formation of indirect tail states, coupling of organic-inorganic moieties and ferroelectricity are reported to be observed in these OIHPs [14–18], which are all believed to influence the electronic structure leading to enhancement of PCE at room temperature. Thus, understanding the mechanism of these phenomena in OIHPs, particularly through their structural origins, is crucial to further tuning their interesting properties.

At ambient pressure, from high temperature to low temperature, MAPbBr₃ transition sequence is cubic (α) to tetragonal-I (β) to tetragonal-II (γ) to orthorhombic (δ) phase [19–21] primarily driven by increasing disorder of MA [20, 22]. The exact nature of the orientational order in the δ and β phase has been under debate with some studies assigning non-polar space groups to these structures [20, 23, 24], while others claiming them to be polar [19, 25, 26]. Notably, a recent study employing a combination of dielectric measurements, pyroelectric current and positive-up-negative-down measurements claimed the existence of polar ferroelectric behaviour along $\langle 001 \rangle$ in the β phase, ruling out the assignment of non-polar $I4/mcm$ space group [26]. However, this claim has been subsequently challenged [27] attributing the observation of pyroelectric current to the presence of metastable polar states. On the other hand, although the high temperature α phase

(>236.9 K) is described as cubic $Pm-3m$ [20, 24, 28, 29], recent studies [30, 31] identified presence of short-range octahedral distortion at room temperature leading to breaking of cubic symmetry. Thus, the exact nature of the structural phases of MAPbBr₃ is as yet unclear, and further work is needed to reconcile seemingly conflicting experimental evidence. In this regard, *ab initio* molecular dynamics (AIMD) based approaches play an important role allowing access to structural and electronic details of the various phases of OIHPs at high spatial and temporal resolution. [32–34].

In this work, we employ AIMD in the isothermal-isobaric ensemble to investigate the nature of the temperature-induced structural phases in MAPbBr₃. We show that, the low-temperature phase is not ferroelectric and is correctly described by the space group $Pnma$. We confirm that while the motion of MA or the inorganic sub-lattice lead to local polar fluctuations at all temperatures, they do not result in an overall polarization. Our simulations at room temperature resulted in a cubic $Pm-3m$ phase with no discernible orthorhombic distortions as proposed in experiments [30, 31]. Our study reveals that the scissoring motion of bromide octahedra leads to a multiple peak feature in the Br-Br pair distribution functions [30] at low temperatures which evolves into a single peak at room temperature. Displacements of the MA ions couple strongly to octahedral distortions through X-H...Br (X=C, N) hydrogen-bonds (H-bonds) evidenced by significant correlation between the relevant order parameters at all temperatures. The timescales of MA motion extracted from our simulations are found to be within good agreement with experiments thereby validating our model and supporting a dynamic disordering of the molecular dipoles via a combination of local angular fluctuations and reorientational jumps. The latter is only significant at 300 K where N-H...Br bonds are frequently broken due to fast rotations about the molecular axis, emphasizing the key role of H-bonds in the dynamics of OIHPs.

* lavanya@barc.gov.in, vardha@iiserb.ac.in

II. COMPUTATIONAL METHODS

Car–Parrinello molecular dynamics [35] simulations were performed using QUANTUM ESPRESSO suite of electronic-structure codes [36]. To accurately model the van der Waals (vdW) interactions in the crystals, we employed the DFT-D2 [37] scheme with a generalized gradient approximation (PBE) [38] to the exchange-correlation functional. Ionic cores were modeled by ultrasoft pseudopotentials[39]. The valence electrons, including the $1s^1$ electron of H, the $2s^2p^2$ electrons of C, the $2s^2p^3$ electrons of N, the $4s^4p^5$ electrons of Br, and the $5d^{10}6s^26p^2$ electrons of Pb were treated explicitly. All simulations were performed using a 768 atom cell in the isothermal-isobaric ensemble (constant NPT) by using the variable-cell Parrinello-Rahman barostat [40] and a single Nose-Hoover thermostat [41] with a frequency of 60 THz to maintain a constant pressure (P) and temperature (T), respectively. All plane waves with kinetic energies below 65 Ry were included and to maintain a constant plane wave kinetic energy cutoff of $E_0 = 55$ Ry for a fluctuating cell, a smooth step function with height $A = 150$ Ry and width $\sigma = 5$ Ry to the plane wave kinetic factor is added as proposed by Bernasconi *et al.* [42]: $G^2 \rightarrow G^2 + A[1 + \text{erf}(\frac{G^2/2 - E_0}{\sigma})]$, where erf is the error function. The augmented charge was represented by the kinetic energy cutoff of 400 Ry. The fictitious mass of the electrons was set to 500 a.u., and a mass preconditioning with a kinetic energy cutoff of 2.5 Ry was used to all Fourier components of wavefunctions [43]. Convergence threshold for electron minimization was chosen as 10^{-6} Ry. A time-step of 10 a.u. (0.242 fs) and actual masses for all atoms are used for ionic propagation.

III. DISTRIBUTION OF MA ORIENTATIONS AND POSSIBILITY OF FERROELECTRICITY IN ORTHORHOMBIC PHASE

The structure of the MAPbBr₃ in any phase is made up of corner-sharing PbBr₆ octahedra with an MA ion associated with every (pseudo-)cubic unit. Each MA ion is expected to align along one of 13 high symmetry directions in the cube. These are classified into 3 groups (see Figure 1(a)) – *face-to-face* (ff), *body diagonal* (bd) and *edge-diagonal* (ed) – corresponding to the 3 C_4 , 4 C_3 and 6 C_2 rotation axes of the cube, respectively. Along with the relative orientation of the C–N bond in MA, these account for 26 possible orientations [44]. In the low temperature δ phase, two groups of MA are oriented approximately along the $\langle 100 \rangle_c$ and $\langle 001 \rangle_c$ pseudo-cubic directions, respectively ($\langle 101 \rangle$ and $\langle 10\bar{1} \rangle$ with respect to the orthorhombic axes). In the $Pnma$ structure, the MA are stacked along the b -axis in an anti-polar fashion giving rise to a net zero dipole moment in the cell. Our DFT-based optimizations employing the van der Waals (vdW) interaction corrected PBE+D2 exchange-correlation (xc) functional [38, 45] yielded the $Pnma$ structure for MAPbBr₃ at 0 K in agreement with previous theoretical findings [27, 46, 47]. The non-ferroelectric ground state thus predicted is robust to variation of the vdW scheme employed or use of hybrid

functionals. Our conclusion agrees with several X-ray diffraction experiments [20, 23, 24] and with more recent reports of lack of ferroelectric switching [27] in the orthorhombic phase. It has been suggested that there may exist local minima slightly higher in energy than the $Pnma$ structure differing from it by small relative rotations and displacements of the MA ions [27]. While these were ruled out in our 0 K optimization studies, we considered their possible occurrence at higher temperatures through our 0 GPa AIMD simulations at 40 K, 180 K and 300 K. To this end we identify the crucial symmetry elements characterizing the MA sub-lattice in the $Pnma$ structure. We first define the polar angles θ and ϕ associated with each MA ion as depicted in Figure 1(b). The orientational distribution plots at 40 K and 180 K (not shown here) indicate that MA rotations are restricted and centred around four sets of polar angles. Assuming a bivariate normal probability distribution function about each set centred at $\mu = (\mu_\theta, \mu_\phi)$ given by:

$$\rho(x) = \frac{1}{2\pi} |\zeta|^{-1/2} \exp \left[-\frac{1}{2} (x - \mu)^T \zeta^{-1} (x - \mu) \right] \quad (1)$$

we use Gaussian Mixture Modelling (GMM) to calculate the equilibrium orientations. At 0 K, the MA are clustered into two groups, v (along $\langle 100 \rangle_c$) and w (along $\langle 001 \rangle_c$), based on the orientation of the MA molecular axis, with an additional index 1 (parallel) or 2 (antiparallel) indicating the alignment of the C→N vector with this axis.

A criteria for the local centrosymmetry between both types (LCM_{12}), in every group described above, is defined as:

$$\mu_\theta(1) + \mu_\theta(2) = 180^\circ \quad (2)$$

$$|\mu_\phi(1) - \mu_\phi(2)| = 180^\circ \quad (3)$$

Similar criteria can also be set for preservation of the four 2_1 screw axes connecting the v and w groups of MA (SM_{vw}) as well as the mirror symmetry elements (MSM) of $Pnma$.

At 40 K the LCM_{12} criteria are satisfied for each of the two groups, v and w , to within 1° indicating MA dipole moments will be canceled due to local centrosymmetry. Along with the preservation of SM_{vw} and MSM criteria this result confirms the assignment of $Pnma$ to the δ phase and, hence, a non-ferroelectric arrangement of MA. We note here that a 768-atom ($4 \times 4 \times 4$) supercell was required to ensure sufficient sampling of the electronic Brillouin zone. A unimodal distribution of the dihedral angle θ_{12} between MA 1 and 2 under v or w group confirms absence of any local energy minima configuration close to the non-ferroelectric arrangement ($\theta_{12}=180^\circ$). We note that, apart from the experimentally suggested non-polar structure, a polar structure with same Pb–Br lattice but parallel stacking of MA ($\theta_{12}=0^\circ$) was also proposed by Sarkar *et al.* [47]. Our optimization starting from the same structure also led to a polar ground state which is only 2 meV/atom higher in energy. However, this structure was not accessed in the 40 K simulations.

At 180 K, both the LCM_{12} and MSM criteria are satisfied suggesting an overall non-polar arrangement of MAs, similar to the iodide perovskite [48]. It should be noted that, to capture the transformation of lattice constants and the “partial

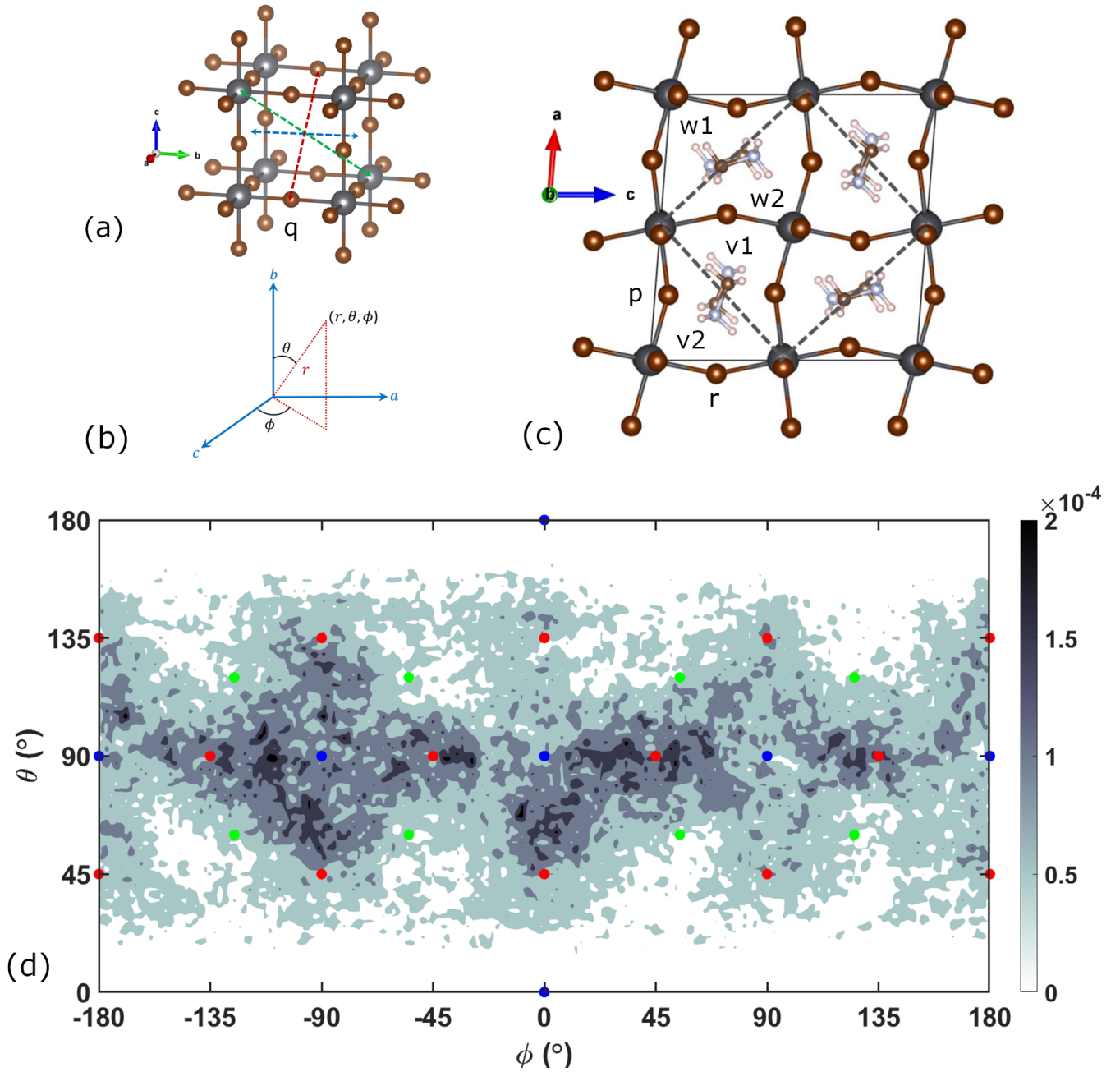


FIG. 1. (a) Structure of the cubic cell where different types of high-symmetry MA orientations are shown. Blue, green and red arrow correspond to ff , bd and ed orientations as described in the text; (b) Choice of order parameter θ and ϕ in polar coordinate system with respect to local axes; (c) Structure of the 48-atom orthorhombic $Pnma$ unit-cell (marked by the dashed boundary) inside (a portion of) the simulation cell; (d) Orientational $(\theta - \phi)$ probability distribution plot of all MA at 300 K. Blue, green and red circles correspond to ff , bd and ed orientations; In (a) and (c), p , q and r label three types of bromines along local (pseudo-)cubic a , b and c axes, respectively.

disorder” of the β phase, a longer simulation is required at 180 K than presently undertaken. Hence, we restrict our focus to the δ and α phases.

At 300 K, the simulations were started on the cubic lattice with MA orientations chosen randomly from the aforementioned 26 possibilities. The orientations subsequently sampled by the AIMD span the whole θ - ϕ space (see Figure 1(d)) with ed orientations being more likely than others, in line with

previous experimental expectations [24]. Among all ff orientations, those along (pseudo-)cubic c axis ($\theta = \pm 180^\circ$) are extremely less sampled, thus creating one strip along the θ axis and four strips along the ϕ axis. At every time step, the MA are categorized into groups based on the least angle they make with the aforementioned 26 orientations, thus obtaining a ratio of occurrence of $ee : ff : bd = 1:0.546:0.397$ indicating the trend in the relative potential depths of these minima. In-

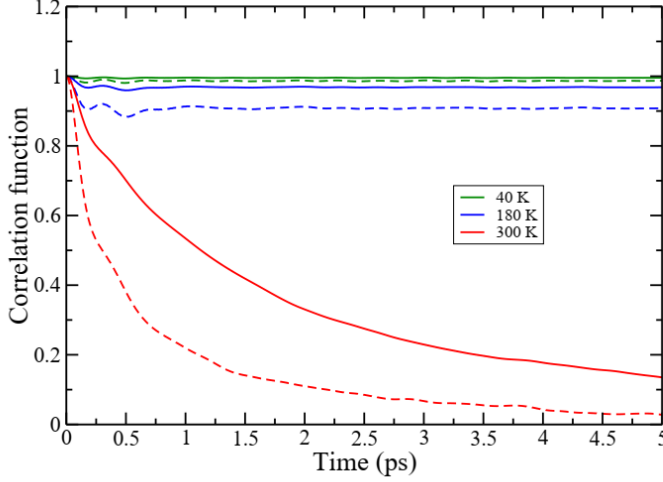


FIG. 2. Correlation functions of C-N motion at 40, 180, and 300 K indicated as green, blue, and red curves. The continuous and dashed curves are for $C_1(t)$ and $C_2(t)$, respectively.

deed, a comparison of DFT energies of these orientations in a cubic unit cell revealed that *ed* is the most stable while *ff* and *bd* are higher in energy by 24 meV/f.u. or more.

Thermal fluctuations about the antipolar stacked MA orientations can generate short-lived local polar configurations as has been reported in some OIHPs [15–17, 49]. Additionally, polarization could also arise from relative displacements of the constituent ions. However, in MAPbBr₃, we find that at 40 and 180 K such displacements either always occur in opposing pairs or do not occur at all, thereby leading to no overall polarization.

IV. DYNAMICS OF MA ORIENTATION

While the MA have been largely believed to show dynamic disorder at 300 K, Page *et al.* [30] suggested the possibility of static disorder where cations can show large fluctuations around their local orientations. Dynamic orientational disorder in MA is confirmed in our work as evidenced by the diffusive nature of the rotational autocorrelation function (ACF) $C_1(t)$ at 300 K shown in Figure 2. The relevant time-scales can be extracted using a general diffusive model proposed by Mattoni *et al.* [50]

$$C_1^M(t) = e^{-t/\tau_0} \left[A_1 + \frac{t}{\tau_0} e^{-(t/\tau_1)^n} + (1 - A_1) \cos\left(\frac{2\pi}{\tau_2} t\right) \frac{1}{(t/\tau_3 + 1)^m} \right] \quad (4)$$

where τ_0 controls the overall exponential decay (particularly that observed at 300 K), τ_1 is the decay time for nearly free rotations occurring at short times, and τ_2 describes the time-scale for harmonic motion with a power-law damping governed by τ_3 . At 40 and 180 K, the ACF show almost no long time decay ($\tau_0 \rightarrow \infty$) confirming their ordered behavior. Note that in the latter phase, reorientation of MA ions leading to

partial disorder is expected but could involve larger (but finite) τ_0 [50] and hence not seen in our 20 ps long simulations. At 300 K, the timescales extracted for the fastest ($\tau_1=341$ fs) and slowest motions ($\tau_0=2.035$ ps) match well with the ssNMR ($\tau_1=355$ fs) [51] and TR-OKE (~ 2 ps) experiments [52].

It has been shown in MAPbI₃ that the dynamics of MAs are governed by a fast ‘wobbling-in-a-cone’ (corresponding to local angular fluctuations) and a slow ‘jump-like’ reorientation motion [53]. In our 300 K simulation of MAPbBr₃, the dynamical disordering of MA orientations over multiple minima (FIG. 1(e)) indicate similar behavior captured by the wobbling-in-a-cone/jump model [54, 55] for which the second order ACF $C_2(t)$ is given by

$$C_2^{WCM}(t) = S^2 e^{-t/\tau_0} + (1 - S^2) e^{-(\frac{1}{\tau_0} + \frac{1}{\tau_1})t} \quad (5)$$

where τ_0 and τ_1 are relaxation times corresponding to the reorientational jump and initial fast motion around a minimum, respectively. S is a generalized order parameter measuring the degree of spatial restriction of motion. The computed $C_2(t)$ can be fit to Eq. 5 to extract $\tau_0 = 1.86$ ps and $\tau_1 = 320$ fs in excellent agreement with corresponding time-scales (1.5 ± 0.3 ps, 300 ± 100 fs) extracted from polarization resolved 2-D IR spectroscopic measurements [56, 57]. Furthermore, τ_0 and τ_1 predicted by both the models are in agreement in line with their expected equivalence. [58].

V. DISTORTIONS IN THE α PHASE

Although the room temperature phase is largely understood to be cubic, some recent studies have suggested the persistence of orthorhombic distortions in this phase manifesting either as orthorhombic lattice parameters [30] or as distorted PbBr₆ octahedra [31]. In either case, the primary evidence is obtained by fitting the radial distribution functions (RDF) from X-ray diffraction data to either a pseudo-cubic (PC) or an orthorhombic (OR) lattice models. In order to verify the possibility of such distortions at 300 K, we estimated the lattice parameters in two ways: by measuring the nearest neighbour Pb-Pb distances (PC) and by using a $\sqrt{2} \times 1 \times \sqrt{2}$ transformed cell tensor (OR). Both the time-averaged PC ($a = 5.978 \pm 0.008$, $b = 5.987 \pm 0.011$, $c = 5.989 \pm 0.016$) and OR ($a = 8.492 \pm 0.060$, $b = 11.973 \pm 0.022$, $c = 8.455 \pm 0.057$) lattice parameters confirm the absence of any significant deviation from cubic symmetry. Thus, cubic models should yield a better fit with experimental data since the presence of local distortions do not manifest through the lattice constant values.

Orthorhombic distortions in the high temperature α -phase were also inferred in experiments from the persistence of a doublet feature in the Br-Br RDF in the 3.5-5 Å region [31]. The evolution of $G(r)\{\text{Br-Br}\}$ with temperature is shown in Figure 3(a) where this doublet is clearly observed up to 180 K. This feature evolves into a broad peak around 4.2 Å at 300 K where the resolution of a doublet, if present, is difficult warranting further investigation into its origin. In any phase, the Br-Br doublet indicates the presence of two distinct Br-Br distances in PbBr₆ octahedra which can arise due to two

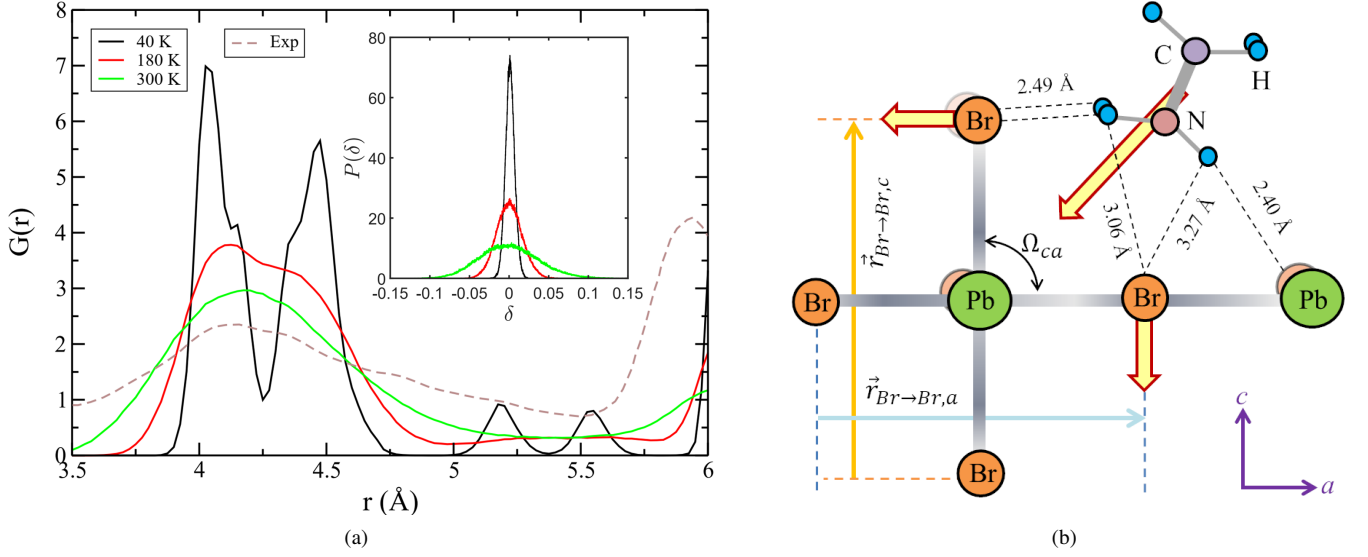


FIG. 3. (a) Evolution of the calculated radial distribution functions of Br-Br pair ($G(r)\{\text{Br-Br}\}$) with temperature in 3.5-5 Å region (continuous lines) along with the total RDF at room temperature taken from experiment [31] (broken line). Inset depicts the evolution of distributions of δ as a measure of tetragonal distortion of octahedra with temperature; (b) Schematic description of the parameters used to calculate δ and Ω distortions. The coupling motion between Ω_{ca} and translation of MA in ca plane is also shown. The distances between $\text{H}\cdots\text{Br}$, shown here for reference, are taken from the 0 K optimized structure.

primary reasons:

- i. a tetragonal distortion defined for the j -th PbBr_6 octahedra as

$$\delta(j, t) = \frac{2 \times |\vec{r}_{\text{Br} \rightarrow \text{Br}, b}(j, t)|}{|\vec{r}_{\text{Br} \rightarrow \text{Br}, a}(j, t)| + |\vec{r}_{\text{Br} \rightarrow \text{Br}, c}(j, t)|} - 1 \quad (6)$$

where, $\vec{r}_{\text{Br} \rightarrow \text{Br}, \mu}(j, t)$ is the vector connecting two Br at opposite vertices of the octahedra situated approximately along the crystal axis μ (see Figure 3(b)), or

- ii. a scissoring distortion measured by the deviation from 90° of the angle between any two $\vec{r}_{\text{Br} \rightarrow \text{Br}, \mu}(j, t)$ in the plane formed by those two vectors

$$\Omega_{\mu\nu}(j, t) = \hat{r}_{\text{Br} \rightarrow \text{Br}, \mu}(j, t) \cdot \hat{r}_{\text{Br} \rightarrow \text{Br}, \nu}(j, t) \quad (7)$$

Distributions of δ at all temperature are unimodal and centered at 0 (inset in Figure 3(a)), indicating the absence of any tetragonal distortion at all temperatures and thus ruling it out as a cause of Br-Br doublet. On the other hand, distributions of the scissoring distortion parameters clearly reveal the origin of doublet-like features. Figure 4(a)-(c) show the distribution of $\Omega_{\mu\nu}(j, t)$ at various temperatures with each peak at a non-zero value corresponding to a Br-Br doublet. At 40 K, there are 5 such peaks whose contribution to the RDF (shown in Figure 4(d)) results in a doublet-like feature emerging primarily from the ϵ peak and partially from κ' . A small splitting of every peak in the doublet occurs due to κ . Along a axis, κ and κ' sit alternately, while their supplementary counterparts (with $\Omega_{ab} < 0$) are situated along b axis. At 180 K, all the

supplementary κ peaks merge at $\Omega = 0$ and only the ϵ peak at $\Omega \neq 0$ yields a Br-Br doublet (see Figure 4(b),(e)). However at 300 K, all the distributions of Ω are unimodal having most probable values at 0 (see Figure 4(c)). Assignment to a single peak was confirmed by a 1-D GMM analysis which found that each of the distributions at 300 K fits best with only a single gaussian component with its mean at zero.

VI. COUPLING OF ORGANIC CATION AND LATTICE

Finally, the coupling between the MA and lattice motion was investigated. To this end, we computed the correlation coefficients $C_T^{\mu\nu}$ between the length of a Pb-Br bond lying along the μ direction and the displacement (from average) of the MA in the ν direction within the same cubic unit cell. Figure 5(a) shows that the coupling of Pb-Br distances and MA translations along the b axis (C_T^{bb}) is reduced with temperature but remains significant even at 300 K. In contrast, we found very little correlation between Pb-Br distances and MA rotations (see Table S10). Interestingly, the scissoring motion in ac plane (Ω_{ac}) and MA translation along the ac edge-diagonal direction $[202]$ are strongly coupled (F_T^{ca}) at 40 K (see Figure 5(a)) primarily due to the H-bonding interactions between the organic and inorganic sub-lattices. As illustrated in Figure 3(b), if Ω_{ac} decreases, the associated scissoring angle increases, thus forcing the MA to translate along the ac edge-diagonal direction towards the origin to maintain the $\text{H}\cdots\text{Br}$ bonds and vice versa. While significant coupling behavior is also seen at 180 and 300 K, this correlation becomes lesser in the cubic phase due to frequent H-bond breaking effected via both MA reorientational jumps as well as rotation about the

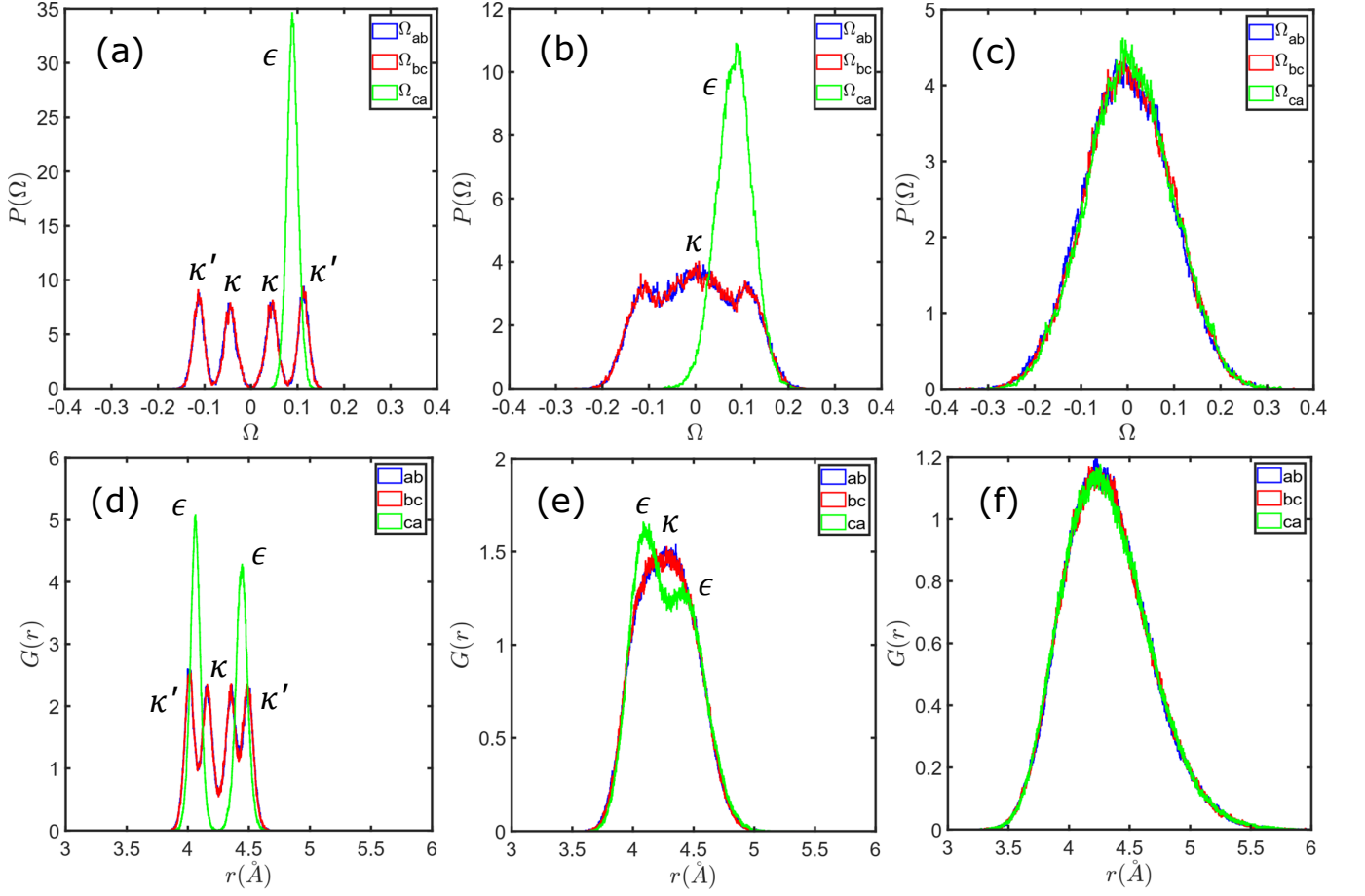


FIG. 4. Distribution of Ω_{ab} , Ω_{bc} and Ω_{ca} as measure of scissoring distortion of octahedra at (a) 40 K, (b) 180 K and (c) 300 K. Plane-wise radial distribution functions arising due to Ω at (d) 40 K, (e) 180 K and (f) 300 K.

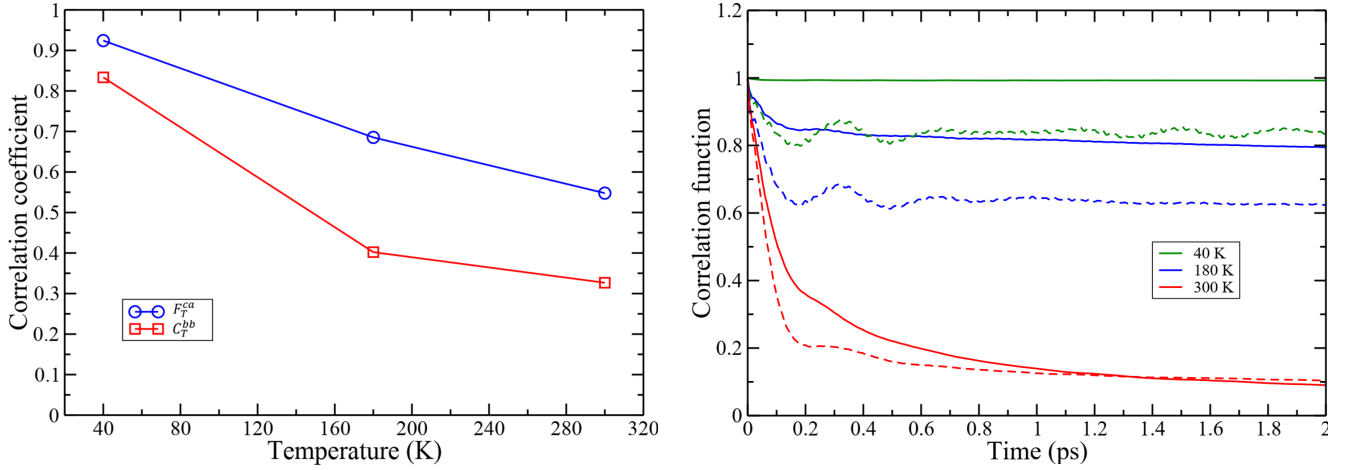


FIG. 5. (a) C_T^{bb} as a measure of coupling of MA translation and Pb-Br bond length along b axis; and F_T^{ca} as a measure of coupling of MA scissoring and MA translation in the ac plane. (b) Time correlation functions of H-bond framework at 40, 180, and 300 K indicated as green, blue, and red curves. The continuous and dashed curves are for N-H...Br and C-H...Br, respectively.

molecular axis. Thus, MA translations couple with the lattice scissoring in the ac plane, whereas translations perpendicular to the plane couple with the corresponding Pb-Br bond stretch

mode. We also note that, at 300 K, Pb-Br bond-length fluctuations on neighbouring unit cells are strongly positively correlated, strengthening the validity of the PC model for lattice

parameters.

Since H-bonds enable the coupling of the two sub-lattices, we also investigated their dynamics. At 40 K N-H \cdots Br and C-H \cdots Br type H-bonds form with H \cdots Br distances up to 2.75 and 3.17 Å, respectively. At 300 K, where dynamic disordering causes H-bonds to break and reform, a peak-like feature for N-H \cdots Br RDF at \sim 2.41 Å confirms the persistence of the H-bond, while the absence of any structure in the C-H \cdots Br RDF suggests that the latter interaction weakens significantly [59]. To probe the dynamical behavior, we construct the following correlation function

$$C_{X-H\cdots Br}(t) = \frac{1}{N} \sum_{i=1}^N \langle \mathbf{H}_i(0) \cdot \mathbf{H}_i(t) \rangle \quad (8)$$

where $\mathbf{H}(t) = [\delta_{X-H\cdots Br_{r_1}}, \dots, \delta_{X-H\cdots Br_{r_{12}}}]$, and $\delta_{X-H\cdots Br}$ equals 1 if the $H \cdots Br$ distance is within the aforementioned distance cutoffs for each type of H-bond or 0 otherwise. Figure 5(b) shows that at all temperatures, the timescale of rotation about MA axis, indicated by the initial rapid decay of $C_{X-H\cdots Br}(t)$, is 0.16 - 0.18 ps in good agreement with experimentally measured value of 0.2 ps [60]. There is no long time decay component in the correlations at 40 and 180 K confirming an ordered H-bonded framework. At 300 K the MA re-orientational jumps significantly reduce the H-bond lifetimes thereby adding a slower component (\sim 2 ps). It should be noted that, at all temperatures, the $C_{C-H\cdots Br}$ functions relax more than $C_{N-H\cdots Br}$ at the fast timescale indicating weaker H-bonding interactions for C than N.

In conclusion, our AIMD simulations in the isothermal-isobaric ensemble clearly establish that the low-temperature

phase of MAPbBr₃ is not ferroelectric and instead conforms to a centrosymmetric space group *Pnma*, while the room temperature phase is cubic (*Pm-3m*) down to the local scale. At 180 K, the MA reorientation dynamics possibly occurs at a much slower timescale than analyzed here. Hence, details of the corresponding phase are not completely captured in our 20 ps trajectory and would require longer simulations. Using time-correlation functions we show that the MA disordering leading to the cubic phase is best described as dynamic with the MA ions thermally diffusing between various orientational minima. The predicted timescales of MA motion agree well with experiments validating this perspective. By designing appropriate order parameters we trace the origins of the experimentally observed doublet feature in Br-Br RDF [31] to a scissoring distortion of the PbBr₆ octahedra. However, this vanishes in our room temperature simulations indicating that no orthorhombic distortions persist in cubic MAPbBr₃. While our simulations indicate the presence of local polar fluctuations arising from the motion of MA, Pb and Br separately, we confirm that they do not lead to any overall polarization at 40, 180, and 300 K. An investigation of the correlations between MA and lattice degrees of freedom indicated that the two subsystems are most strongly coupled through displacements of the MA ion through all temperatures. MA translations correlate with the lattice scissoring in *ac* plane but with Pb-Br bond lengths in the *b* direction, thus indicating an anisotropic coupling enabled by H-bonding. An analysis of H-bond lifetimes yielded timescales similar to those involved in MA rotational and motion emphasising the importance of the H-bonding in controlling the order-disorder transition of the MA sub-system.

-
- [1] A. Kojima, K. Teshima, Y. Shirai, and T. Miyasaka, Novel photoelectrochemical cell with mesoscopic electrodes sensitized by lead-halide compounds (2), in *Proc. 210th ECS Meeting* (2006) p. 1.
 - [2] A. Kojima, K. Teshima, Y. Shirai, and T. Miyasaka, Organometal halide perovskites as visible-light sensitizers for photovoltaic cells, *Journal of the American Chemical Society* **131**, 6050 (2009).
 - [3] J.-H. Im, C.-R. Lee, J.-W. Lee, S.-W. Park, and N.-G. Park, 6.5% efficient perovskite quantum-dot-sensitized solar cell, *Nanoscale* **3**, 4088 (2011).
 - [4] H.-S. Kim, C.-R. Lee, J.-H. Im, K.-B. Lee, T. Moehl, A. Marchioro, S.-J. Moon, R. Humphry-Baker, J.-H. Yum, J. E. Moser, *et al.*, Lead iodide perovskite sensitized all-solid-state submicron thin film mesoscopic solar cell with efficiency exceeding 9%, *Scientific reports* **2**, 1 (2012).
 - [5] M. M. Lee, J. Teuscher, T. Miyasaka, T. N. Murakami, and H. J. Snaith, Efficient hybrid solar cells based on meso-structured organometal halide perovskites, *Science* **338**, 643 (2012).
 - [6] L. Etgar, P. Gao, Z. Xue, Q. Peng, A. K. Chandiran, B. Liu, M. K. Nazeeruddin, and M. Grätzel, Mesoscopic $\text{CH}_3\text{NH}_3\text{PbI}_3/\text{TiO}_2$ heterojunction solar cells, *Journal of the American Chemical Society* **134**, 17396 (2012).
 - [7] Q. Chen, H. Zhou, Z. Hong, S. Luo, H.-S. Duan, H.-H. Wang, Y. Liu, G. Li, and Y. Yang, Planar heterojunction perovskite solar cells via vapor-assisted solution process, *Journal of the American Chemical Society* **136**, 622 (2014).
 - [8] J.-Y. Jeng, Y.-F. Chiang, M.-H. Lee, S.-R. Peng, T.-F. Guo, P. Chen, and T.-C. Wen, $\text{CH}_3\text{NH}_3\text{PbI}_3$ perovskite/fullerene planar-heterojunction hybrid solar cells, *Advanced Materials* **25**, 3727 (2013).
 - [9] M. Liu, M. B. Johnston, and H. J. Snaith, Efficient planar heterojunction perovskite solar cells by vapour deposition, *Nature* **501**, 395 (2013).
 - [10] J. H. Noh, S. H. Im, J. H. Heo, T. N. Mandal, and S. I. Seok, Chemical management for colorful, efficient, and stable inorganic-organic hybrid nanostructured solar cells, *Nano letters* **13**, 1764 (2013).
 - [11] N.-G. Park, Organometal perovskite light absorbers toward a 20% efficiency low-cost solid-state mesoscopic solar cell, *The Journal of Physical Chemistry Letters* **4**, 2423 (2013).
 - [12] D. Liu and T. L. Kelly, Perovskite solar cells with a planar heterojunction structure prepared using room-temperature solution processing techniques, *Nature photonics* **8**, 133 (2014).
 - [13] A. Kogo, Y. Sanehira, Y. Numata, M. Ikegami, and T. Miyasaka, Amorphous metal oxide blocking layers for highly efficient low-temperature brookite TiO_2 -based perovskite solar cells, *ACS applied materials & interfaces* **10**, 2224 (2018).
 - [14] T. Etienne, E. Mosconi, and F. De Angelis, Dynamical origin

- of the rashba effect in organohalide lead perovskites: A key to suppressed carrier recombination in perovskite solar cells?, *The journal of physical chemistry letters* **7**, 1638 (2016).
- [15] A. N. Beecher, O. E. Semonin, J. M. Skelton, J. M. Frost, M. W. Terban, H. Zhai, A. Alatas, J. S. Owen, A. Walsh, and S. J. Billinge, Direct observation of dynamic symmetry breaking above room temperature in methylammonium lead iodide perovskite, *ACS energy Letters* **1**, 880 (2016).
- [16] P. Guo, Y. Xia, J. Gong, C. C. Stoumpos, K. M. McCall, G. C. Alexander, Z. Ma, H. Zhou, D. J. Gosztola, J. B. Ketterson, *et al.*, Polar fluctuations in metal halide perovskites uncovered by acoustic phonon anomalies, *ACS Energy Letters* **2**, 2463 (2017).
- [17] O. Yaffe, Y. Guo, L. Z. Tan, D. A. Egger, T. Hull, C. C. Stoumpos, F. Zheng, T. F. Heinz, L. Kronik, M. G. Kanatzidis, *et al.*, Local polar fluctuations in lead halide perovskite crystals, *Physical review letters* **118**, 136001 (2017).
- [18] B. Wu, H. Yuan, Q. Xu, J. A. Steele, D. Giovanni, P. Puech, J. Fu, Y. F. Ng, N. F. Jamaludin, A. Solanki, *et al.*, Indirect tail states formation by thermal-induced polar fluctuations in halide perovskites, *Nature communications* **10**, 1 (2019).
- [19] A. Poglitsch and D. Weber, Dynamic disorder in methylammoniumtrihalogenoplumbates (ii) observed by millimeter-wave spectroscopy, *The Journal of chemical physics* **87**, 6373 (1987).
- [20] I. Swainson, R. Hammond, C. Soullière, O. Knop, and W. Massa, Phase transitions in the perovskite methylammonium lead bromide, *ch3nh3pbbr3*, *Journal of Solid State Chemistry* **176**, 97 (2003).
- [21] Q. Chen, N. De Marco, Y. M. Yang, T.-B. Song, C.-C. Chen, H. Zhao, Z. Hong, H. Zhou, and Y. Yang, Under the spotlight: The organic-inorganic hybrid halide perovskite for optoelectronic applications, *Nano Today* **10**, 355 (2015).
- [22] H. Mashiyama, Y. Kawamura, H. Kasano, T. Asahi, Y. Noda, and H. Kimura, Disordered configuration of methylammonium of *ch3nh3pbbr3* determined by single crystal neutron diffraction, *Ferroelectrics* **348**, 182 (2007).
- [23] D. Niesner, M. Wilhelm, I. Levchuk, A. Osvet, S. Shrestha, M. Batentschuk, C. Brabec, and T. Fauster, Giant rashba splitting in *ch 3 nh 3 pbbr 3* organic-inorganic perovskite, *Physical review letters* **117**, 126401 (2016).
- [24] C. A. López, M. V. Martínez-Huerta, M. C. Alvarez-Galván, P. Kayser, P. Gant, A. Castellanos-Gomez, M. T. Fernández-Díaz, F. Fauth, and J. A. Alonso, Elucidating the methylammonium (ma) conformation in *mapbbr3* perovskite with application in solar cells, *Inorganic chemistry* **56**, 14214 (2017).
- [25] K. Gesi, Effect of hydrostatic pressure on the structural phase transitions in *ch3nh3pbx3* (*x*= cl, br, i), *Ferroelectrics* **203**, 249 (1997).
- [26] Z.-R. Gao, X.-F. Sun, Y.-Y. Wu, Y.-Z. Wu, H.-L. Cai, and X. Wu, Ferroelectricity of the orthorhombic and tetragonal *mapbbr3* single crystal, *The journal of physical chemistry letters* **10**, 2522 (2019).
- [27] A. G. Lehmann, F. Congiu, D. Marongiu, A. Mura, A. Filippetti, A. Mattoni, M. Saba, G. Pegna, V. Sarritzu, F. Quochi, *et al.*, Long-lived electrets and lack of ferroelectricity in methylammonium lead bromide *ch 3 nh 3 pbbr 3* ferroelastic single crystals, *Physical Chemistry Chemical Physics* **23**, 3233 (2021).
- [28] Y. Rakita, E. Meirzadeh, T. Bendikov, V. Kalchenko, I. Lubomirsky, G. Hodes, D. Ehre, and D. Cahen, *Ch3nh3pbbr3* is not pyroelectric, excluding ferroelectric-enhanced photovoltaic performance, *APL Materials* **4**, 051101 (2016).
- [29] K. Brown, S. Parker, I. R. García, S. Mukhopadhyay, V. G. Sakai, and C. Stock, Molecular orientational melting within a lead-halide octahedron framework: The order-disorder transition in *ch 3 nh 3 pbbr 3*, *Physical Review B* **96**, 174111 (2017).
- [30] K. Page, J. E. Siewenie, P. Quadrelli, and L. Malavasi, Short-range order of methylammonium and persistence of distortion at the local scale in *mapbbr3* hybrid perovskite, *Angewandte Chemie International Edition* **55**, 14320 (2016).
- [31] A. Bernasconi and L. Malavasi, Direct evidence of permanent octahedra distortion in *mapbbr3* hybrid perovskite, *ACS Energy Letters* **2**, 863 (2017).
- [32] E. Mosconi, C. Quarti, T. Ivanovska, G. Ruani, and F. De Angelis, Structural and electronic properties of organo-halide lead perovskites: a combined ir-spectroscopy and ab initio molecular dynamics investigation, *Physical Chemistry Chemical Physics* **16**, 16137 (2014).
- [33] C. Quarti, E. Mosconi, and F. De Angelis, Structural and electronic properties of organo-halide hybrid perovskites from ab initio molecular dynamics, *Physical Chemistry Chemical Physics* **17**, 9394 (2015).
- [34] C. Quarti, E. Mosconi, and F. De Angelis, Interplay of orientational order and electronic structure in methylammonium lead iodide: implications for solar cell operation, *Chemistry of Materials* **26**, 6557 (2014).
- [35] R. Car and M. Parrinello, Unified approach for molecular dynamics and density-functional theory, *Physical review letters* **55**, 2471 (1985).
- [36] P. Giannozzi, S. Baroni, N. Bonini, M. Calandra, R. Car, C. Cavazzoni, D. Ceresoli, G. L. Chiarotti, M. Cococcioni, I. Dabo, *et al.*, Quantum espresso: a modular and open-source software project for quantum simulations of materials, *Journal of physics: Condensed matter* **21**, 395502 (2009).
- [37] S. Grimme, Semiempirical gga-type density functional constructed with a long-range dispersion correction, *Journal of Computational Chemistry* **27**, 1787 (2006).
- [38] J. P. Perdew, K. Burke, and M. Ernzerhof, Generalized gradient approximation made simple, *Phys. Rev. Lett.* **77**, 3865 (1996).
- [39] D. Vanderbilt, Soft self-consistent pseudopotentials in a generalized eigenvalue formalism, *Phys. Rev. B* **41**, 7892 (1990).
- [40] M. Parrinello and A. Rahman, Crystal structure and pair potentials: A molecular-dynamics study, *Physical review letters* **45**, 1196 (1980).
- [41] G. J. Martyna, M. L. Klein, and M. Tuckerman, Nosé-hoover chains: The canonical ensemble via continuous dynamics, *The Journal of chemical physics* **97**, 2635 (1992).
- [42] M. Bernasconi, G. Chiarotti, P. Focher, S. Scandolo, E. Tosatti, and M. Parrinello, First-principle-constant pressure molecular dynamics, *Journal of Physics and Chemistry of Solids* **56**, 501 (1995).
- [43] F. Tassone, F. Mauri, and R. Car, Acceleration schemes for ab initio molecular-dynamics simulations and electronic-structure calculations, *Physical Review B* **50**, 10561 (1994).
- [44] N. Onoda-Yamamuro, T. Matsuo, and H. Suga, Calorimetric and ir spectroscopic studies of phase transitions in methylammonium trihalogenoplumbates (ii), *Journal of Physics and Chemistry of Solids* **51**, 1383 (1990).
- [45] S. Grimme, Semiempirical gga-type density functional constructed with a long-range dispersion correction, *Journal of computational chemistry* **27**, 1787 (2006).
- [46] I. Swainson, M. Tucker, D. Wilson, B. Winkler, and V. Milman, Pressure response of an organic-inorganic perovskite: methylammonium lead bromide, *Chemistry of materials* **19**, 2401 (2007).
- [47] S. Sarkar and P. Mahadevan, Role of the a-site cation in determining the properties of the hybrid perovskite *ch 3 nh 3 pbbr 3*, *Physical Review B* **95**, 214118 (2017).

- [48] J. Breternitz, F. Lehmann, S. Barnett, H. Nowell, and S. Schorr, Role of the iodide–methylammonium interaction in the ferroelectricity of $\text{CH}_3\text{NH}_3\text{PbI}_3$, *Angewandte Chemie International Edition* **59**, 424 (2020).
- [49] G. Laurita, D. H. Fabini, C. C. Stoumpos, M. G. Kanatzidis, and R. Seshadri, Chemical tuning of dynamic cation off-centering in the cubic phases of hybrid tin and lead halide perovskites, *Chemical science* **8**, 5628 (2017).
- [50] A. Mattoni, A. Filippetti, M. Saba, and P. Delugas, Methylammonium rotational dynamics in lead halide perovskite by classical molecular dynamics: the role of temperature, *The Journal of Physical Chemistry C* **119**, 17421 (2015).
- [51] R. E. Wasylshen, O. Knop, and J. B. Macdonald, Cation rotation in methylammonium lead halides, *Solid state communications* **56**, 581 (1985).
- [52] H. Zhu, K. Miyata, Y. Fu, J. Wang, P. P. Joshi, D. Niesner, K. W. Williams, S. Jin, and X.-Y. Zhu, Screening in crystalline liquids protects energetic carriers in hybrid perovskites, *Science* **353**, 1409 (2016).
- [53] A. A. Bakulin, O. Selig, H. J. Bakker, Y. L. Rezus, C. Müller, T. Glaser, R. Lovrincic, Z. Sun, Z. Chen, A. Walsh, *et al.*, Real-time observation of organic cation reorientation in methylammonium lead iodide perovskites, *The journal of physical chemistry letters* **6**, 3663 (2015).
- [54] M. Ji and K. J. Gaffney, Orientational relaxation dynamics in aqueous ionic solution: Polarization-selective two-dimensional infrared study of angular jump-exchange dynamics in aqueous 6M NaClO_4 , *The Journal of chemical physics* **134**, 044516 (2011).
- [55] G. Lipari and A. Szabo, Model-free approach to the interpretation of nuclear magnetic resonance relaxation in macromolecules. 1. theory and range of validity, *Journal of the American Chemical Society* **104**, 4546 (1982).
- [56] O. Selig, A. Sadhanala, C. Müller, R. Lovrincic, Z. Chen, Y. L. Rezus, J. M. Frost, T. L. Jansen, and A. A. Bakulin, Organic cation rotation and immobilization in pure and mixed methylammonium lead-halide perovskites, *Journal of the American Chemical Society* **139**, 4068 (2017).
- [57] Y.-S. Lin, P. Pieniazek, M. Yang, and J. Skinner, On the calculation of rotational anisotropy decay, as measured by ultrafast polarization-resolved vibrational pump-probe experiments, *The Journal of chemical physics* **132**, 174505 (2010).
- [58] A. Mattoni, A. Filippetti, and C. Caddeo, Modeling hybrid perovskites by molecular dynamics, *Journal of Physics: Condensed Matter* **29**, 043001 (2016).
- [59] T. Yin, Y. Fang, X. Fan, B. Zhang, J.-L. Kuo, T. J. White, G. M. Chow, J. Yan, and Z. X. Shen, Hydrogen-bonding evolution during the polymorphic transformations in $\text{CH}_3\text{NH}_3\text{PbBr}_3$: experiment and theory, *Chemistry of Materials* **29**, 5974 (2017).
- [60] G. M. Bernard, R. E. Wasylshen, C. I. Ratcliffe, V. Ter-skikh, Q. Wu, J. M. Buriak, and T. Hauger, Methylammonium cation dynamics in methylammonium lead halide perovskites: A solid-state nmr perspective, *The Journal of Physical Chemistry A* **122**, 1560 (2018).